small NANO MICRO

Multimaterial nanostructures

Mimicking Electrodeposition in the Gas Phase: A Programmable Concept for Selected-Area Fabrication of Multimaterial Nanostructures

*Jesse J. Cole, En-Chiang Lin, Chad R. Barry, and Heiko O. Jacobs**

An in situ gas-phase process that produces charged streams of Au, Si, TiO_2, ZnO, and Ge nanoparticles/clusters is reported together with a programmable concept for selected-area assembly/printing of more than one material type. The gas-phase process mimics solution electrodeposition whereby ions in the liquid phase are replaced with charged clusters in the gas phase. The pressure range in which the analogy applies is discussed and it is demonstrated that particles can be plated into pores vertically (minimum resolution 60 nm) or laterally to form low-resistivity (48 $\mu\Omega$ cm) interconnects. The process is applied to the formation of multimaterial nanoparticle films and sensors. The system works at atmospheric pressure and deposits material at room temperature onto electrically biased substrate regions. The combination of pumpless operation and parallel nozzle-free deposition provides a scalable tool for printable flexible electronics and the capability to mix and match materials.

Keywords:
- clusters
- electrodeposition
- interconnects
- nanostructures
- sensors

1. Introduction

Modern interest in nanotechnology as a platform for functional systems drives the need for techniques to localize deposition of metals, oxides, and semiconducting materials. From a synthesis point of view, these materials are commonly formed in the liquid or gas phase. One of the most powerful liquid-phase techniques remains traditional electrodeposition, which has several unique characteristics absent from emerging direct write[1–3] or transfer techniques.[4] The most important is the ability to locally program the deposition of material (ions,[5] nanoparticles,[6,7] and nanowires[8]) by simply applying a bias to an electrode.[9,10] This characteristic supports the programmable selected-area deposition of materials and is presently limited to the liquid phase. The closest known gas-phase extension to electrodeposition is the use of electrostatic precipitators,[11] which employ electrically biased plates to attract charged particles for filter applications. A gas-phase deposition system to deposit material into addressable areas forming vias, interconnects, patterned multimaterial, or multilayer films in a programmable fashion has, however, not yet been reported. Such a deposition process would be important in the context of printable electronics since many functional nanomaterials are presently formed in the gas phase.

The present report describes a system working at atmospheric pressure to form electrically interconnected nanostructured thin films with 60 nm lateral resolution and predetermined thickness. The system uses a dc plasma arc discharge between two consumable electrodes as a material source. The use of a dc arc discharge between consumable electrodes is a known concept to produce charged nanomaterials in large quantities. A dc arc discharge between graphite electrodes led to the discovery and industrial production of fullerenes and carbon nanotubes,[12–15] and the concept has also been extended to produce GaN,[16] Pd,[17] and Si[18] clusters and particles to name but a few. In these earlier systems, particles coated the reactor walls uniformly.

Herein, we describe an in situ method that couples the particle source with a localized deposition system to mimic

[*] Prof. H. O. Jacobs, J. J. Cole,[+] E.-C. Lin,[+] Dr. C. R. Barry
Electrical Engineering
University of Minnesota
Rm. 4-178, 200 Union St. SE, Minneapolis, MN 55455 (USA)
E-mail: hjacobs@umn.edu
[+] These authors contributed equally to this work.

Supporting Information is available on the WWW under http://www.small-journal.com or from the author.

DOI: 10.1002/smll.200901547

electrodeposition in a gaseous environment. The approach uses a patterned substrate to funnel the material to specific locations with 60 nm standard deviation in positional accuracy, and uses an array of electrically biased domains to sequentially program the deposition of more than one material type. This is different from prior work in the field of gas-phase nanoxerography, in which nanoparticles were deposited onto charged substrate locations using a fixed amount of initial charge inside a dielectric[19] or a p–n junction.[20] These prior methods do not allow programming. Moreover, the fixed amount of initial charge limits the quantity of charged material that can be attracted before the trapped charges are depleted and screened. In the present case, the biased electrodes provide a path for charge neutralization and maintain a constant potential difference that directs the assembly until the external voltage is turned off. This provides control over the amount and type of material that can be deposited onto a desired area. As an application, programmable selected-area deposition of dissimilar materials is used to fabricate physical sensor arrays containing light- and humidity-sensitive areas on the same chip. The physics of how the particles are charged in the particular arc discharge system prior to deposition on a substrate at room temperature is discussed. It involves diffusional charging through a positive space-charge region surrounding the electrode, which is consumed by the process to form charged nanoclusters that finally deposit on a low-temperature substrate.

2. Results and Discussion

Figure 1 illustrates the basic elements and dimensions of the apparatus. It uses a 0.1–100 mA dc plasma arc discharge between two consumable electrodes (left side of Figure 1A,B) to continuously generate nanoparticles and a third sample electrode placed in the region outside of the visible plasma volume (aerosol region) to collect 20 nm Au, 15 nm Si, 15 nm TiO_2, 15 nm ZnO, or 10 nm Ge nanoparticles (right side of Figure 1A,B). Nanoparticle collection is discussed later in Figure 3C and Figure 5D. Additional details for the apparatus used here are included in the Experimental Section. The anode (Figure 1B, top electrode) was given a high positive potential and the cathode (Figure 1B, bottom) was electrically grounded. The upper right inset in Figure 1B shows a typical current–voltage (*I–V*) arc characteristic for Si electrodes with a 2 mm gap distance. We operated the system in the arc regime to the right, which is characterized by the negative differential resistance as opposed to the corona regime to the left. Photographs of the arc (Figure 1B, lower inset) were taken at 10× reduced arc power (1 mA, 1 kV, and 1 W) to resolve the electrode, and show the expected blue-white arc luminescence for atmospheric-pressure air conditions (21% O_2 and 78% N_2 by mole) and red-purple arc luminescence (not shown) after argon purging (>99.9% Ar). Arc luminescence indicates positive ionization of gaseous species.[21]

The process of nanoparticle formation using atmospheric-pressure arcs is well established and we refer to Smirnov[22] for an introduction. In brief, high-mobility electrons generated by the arc are accelerated by the applied electric field to the anode, thus producing gas ions as they travel. Incident positive gas ions are brought to the cathode where they impact the cathode tip surface. Erosion is observed only at the cathode because the heavy positive gas ions will release more kinetic energy than the electrons when impacting the electrode surface. The erosion process increases with the arc current.[23]

Figure 2 provides material-specific data to represent a few of the nanomaterials that are formed as a result of cathode erosion at an input power that was limited to 10 W to prevent rapid evaporation of the cathodes. The results confirm that the dc arc discharge can quickly be adapted to produce a variety of materials that are considered important in the field of printable electronics. The average particle sizes were found to be 20 nm for Au, 15 nm for Si, 10 nm for Ge, 15 nm for TiO_2, and 15 nm for ZnO. Energy-dispersive X-ray spectroscopy (EDX) of Si and ZnO nanoparticles shows the presence of oxygen in addition to

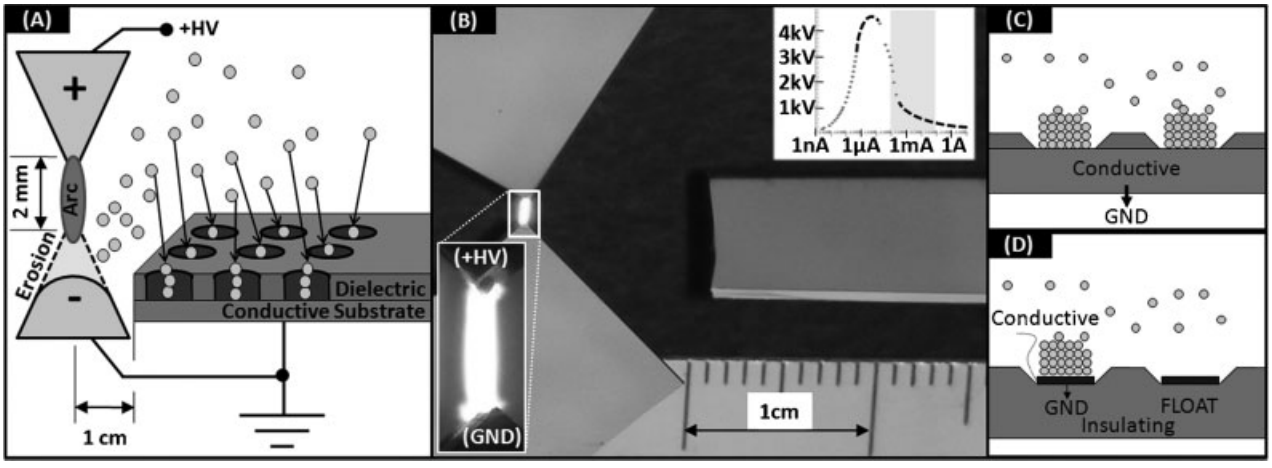

Figure 1. Schematics and photograph of the basic elements of the prototype gas-phase nanocluster electrodeposition system. A) An atmospheric-pressure dc arc discharge is established between two consumable electrodes that are separated by 2 mm. B) Photograph and zoom showing the typical appearance of the arc between silicon electrodes, where the cathode at the bottom, which is initially sharp, is rounded and consumed over time. Inset, top: The arc is operated within the negative differential resistance regime highlighted in the recorded *I–V* characteristic, which is accomplished using a current-controlled high-voltage source as opposed to the positive differential resistance corona discharge region to the left. The nanoparticles

small NANO MICRO

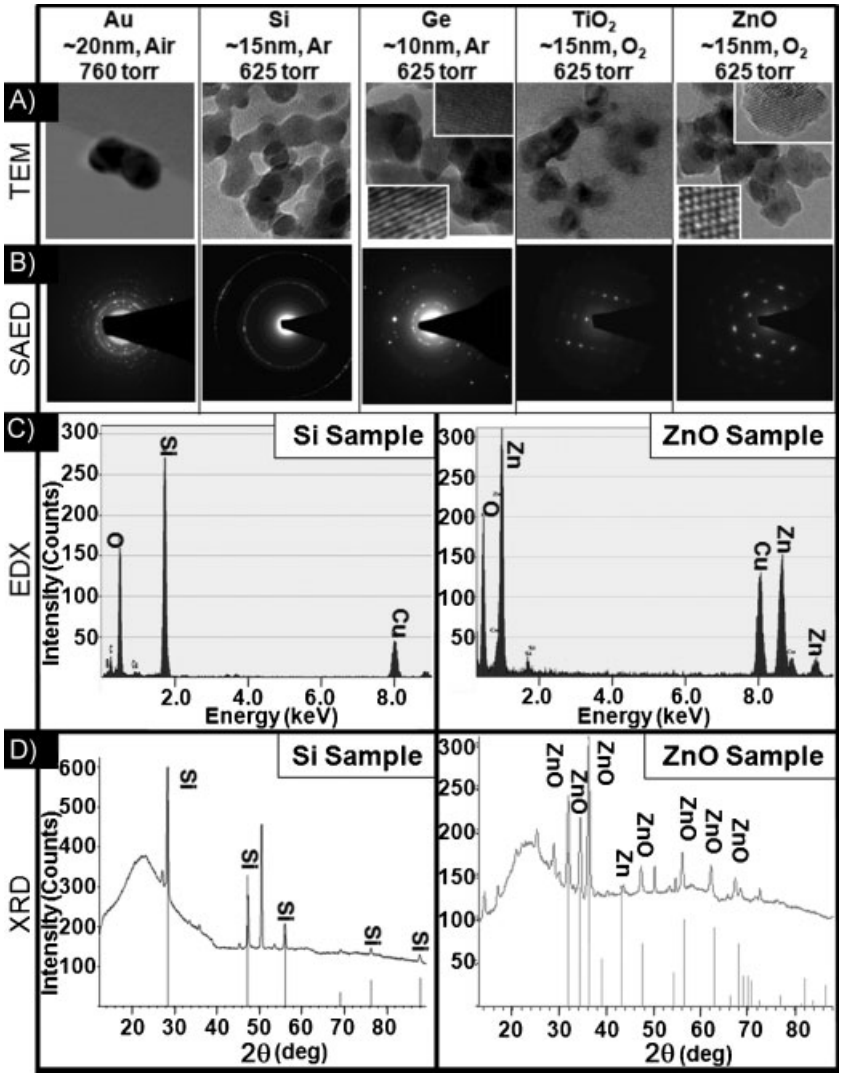

Figure 2. Characterization of nanomaterials produced by an atmospheric-pressure arc discharge. A) Transmission electron microscopy (TEM) results show that sub-20-nm nanoparticles of Au, Si, Ge, TiO_2, and ZnO were generated, with high-resolution TEM images (insets) showing fringes for Ge and ZnO particles. B) Selected-area electron diffraction (SAED) confirms high particle crystallinity in all cases. C) EDX results for Si and ZnO suggest the nanoparticle material type was related to the arc electrode material, with a noticeable oxygen presence in its surface-sensitive signal. D) XRD data confirm strong unoxidized Si peaks suggesting minimal oxidation of Si nanoparticle interiors, which contrasts with the nearly complete oxidation of Zn into ZnO.

the electrode material. X-ray diffraction (XRD), which is sensitive to material deeper than the surface, shows strong Si peaks and the absence of any significant SiO_2, which suggests that the Si particles have crystalline Si cores with SiO_2 surfaces. This contrasts with the case when Zn electrodes were used; here, XRD suggests nearly complete oxidation to produce ZnO in the semiconducting zincite form. The Supporting Information provides further discussion and includes results for Au, Ge, and TiO_2.

Figure 3 depicts the working hypothesis of the deposition process and provides details as to why the particles become positively charged, which supports collection on grounded or negatively biased conducting surfaces. The upper illustration describes the case for metal electrodes (M) exposed to an argon dc arc discharge, but it can be extended to all the other materials and carrier gases that we have investigated so far. The illustration at the top of Figure 3 is divided into three areas: A) a hot plasma region with free electrons e^-, Ar^+ ions, and positive particles M^+ of concentrations n_e, n_i, and n_m, respectively, which is quasineutral ($n_e = n_i + n_m$); B) a warm transitional region, and C) a cold aerosol region where the positive particle/ion concentration $n_i + n_m$ exceeds the free-electron concentration n_e forming a positively charge aerosol ($n_e << n_i + n_m$). The cold aerosol region depicts a flux of positively charged particles M^+ and ions Ar^+, which is recorded using an electrometer.

Visual inspection of the consumable electrodes shows that the nanoparticles originate at the cathode, which is eroded and consumed over time while the anode remains largely unaffected by the process. The nanoparticles diffuse through the transition region and deposit onto grounded surfaces causing discoloration visible to the naked eye within a minute. However, the nanoparticles will not coat insulating surfaces. This selectivity between conducting and insulating surfaces is illustrated in the schematic and scanning electron microscopy (SEM) images in Figure 3D–G. The materials are deposited into 300-nm openings in a 100-nm-thick insulating film of poly(methyl methacrylate) (PMMA) resist on top of a grounded Si chip to form towerlike structures (Figure 3E,G) as the deposition continues. During deposition a positive net ion current is recorded using the electrometer (Keithley, model 6517A) in the range of 0.1–20 nA, where 5 nA is a typical value. This current is related to the M^+ deposition rate. For example, if we operate the system in the corona discharge regime this current drops by two orders of magnitude, which is reflected in a reduced deposition rate. The durations to develop the pattern were 2 min for Figure 3F and 15 min for Figure 3G, both using a deposition current of 5 nA and yielding an average deposition rate of $\approx$70 nm min^{-1}.

We observe positive charging of nanoparticles, which is somewhat counterintuitive from a plasma physics standpoint.[24] In a plasma, surfaces typically acquire a negative surface charge since the electron thermal velocity $\sqrt{[3T_e/m]}$ exceeds the positive gas ion thermal velocity $\sqrt{[3T_i/M]}$ in thermal equilibrium $T_e = T_i$ by roughly three orders of magnitude due to the smaller electron mass m. However, this negative surface charge is compensated by a sheath of positive space charge, as illustrated in the pink region of Figure 3A.[25–27] Particles that originate at the cathode transit through this

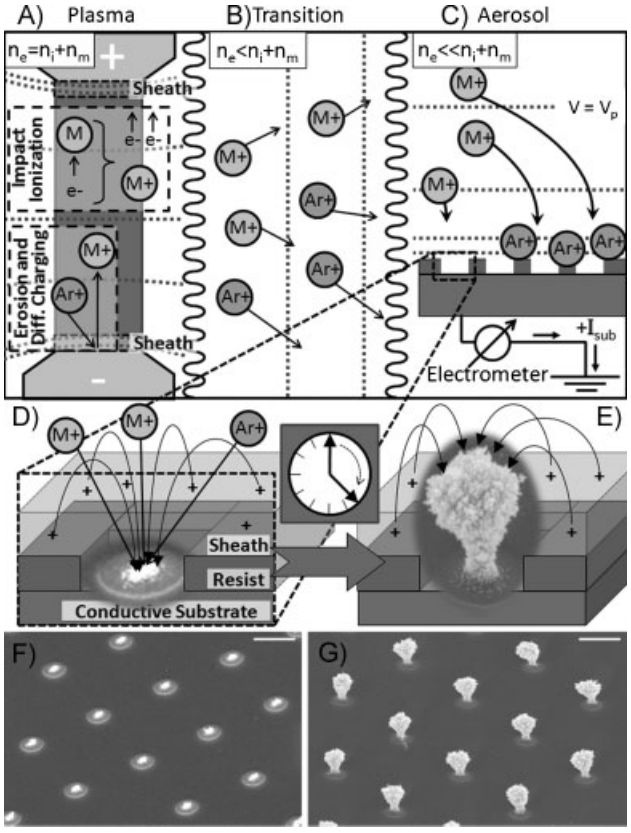

Figure 3. Process details and hypothesis. A) Nanomaterials in the arc become charged as they leave the positively charged cathode sheath (pink layer) and diffuse away through a B) transitional region before entering a C) cold aerosol region where they are collected. The collection of M^+ and Ar^+ ions in (C) is monitored using an electrometer that connects the sample to ground and records the steady-state neutralization current. D,E) The nanolens effect visible in the overlaid SEM results is explained by using high-mobility Ar^+ gas ions, which cause the patterned dielectric layer (purple) to float up and become positively charged (pink transparent sheath layer). The lower-mobility nanoparticles (Au shown) deposit in the openings as a result of the established fringing field. Continuous nanoparticle deposition develops the pattern into towerlike structures. F,G) SEM images. Scale bars: 1 μm.

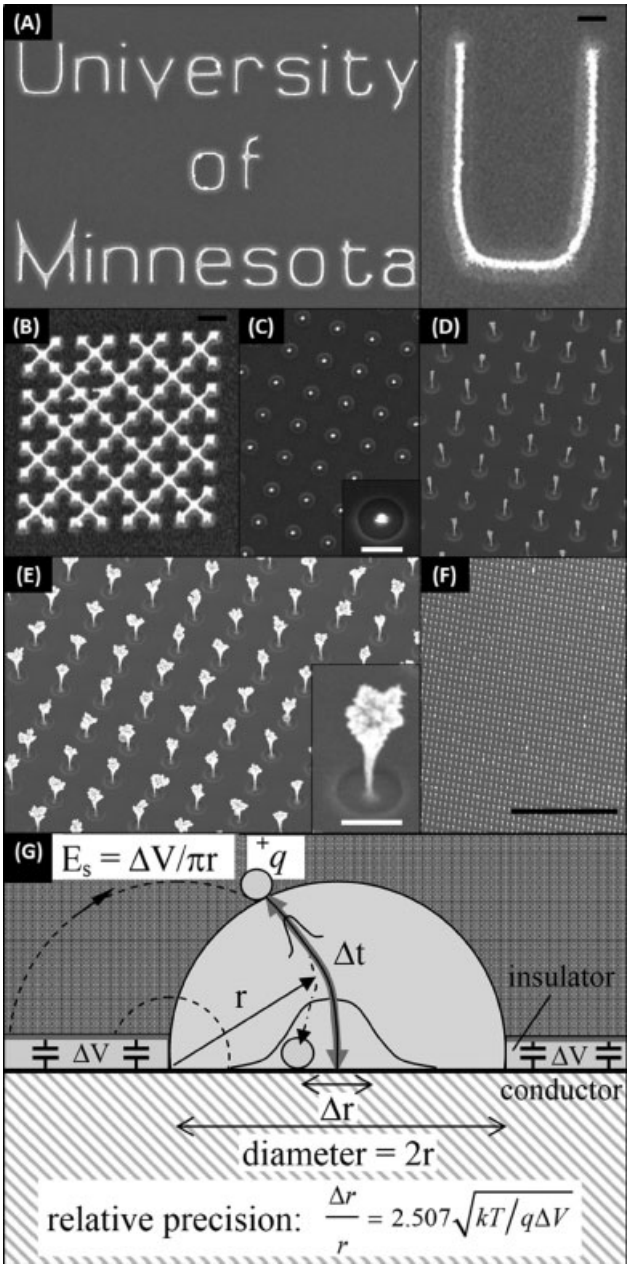

Figure 4. Representative images of nanoparticle deposits limited to Au as a function of deposition time increasing from 2 (A–C) to 15 (D) to 30 min (E,F) at a constant arc discharge power of 10 W. Particles deposit into openings in 80-nm thin PMMA electron-beam resist (A,B) or 0.5-μm-thick Shipley 1805 photoresist (D–F) with a minimal lateral resolution of 60 nm. Particles do not deposit on the resist and are initially directed to the centers of resist openings (G). Scale bars: A inset): 100 nm, B): 1 μm, C, E insets): 1 μm, and F): 100 μm.

region and acquire a net positive charge (Figure 3A, bottom inset) through diffusion charging.[28] Electron-impact ionization[29] is a second major charging mechanism that may play a role as well (Figure 3A, top inset). The charged particles will leave the arc vicinity crossing isopotential lines (dotted gray lines) driven by thermophoresis diffusion and convection to ultimately encounter the sample (Figure 3C), where they deposit on grounded or negatively biased surfaces.

Figure 4 depicts this selectivity between conducting and insulating surfaces, and shows gas-phase plating of <20 nm gold particles to form text, interconnected lines, grids, and arrays of vertical deposits on a silicon substrate that was partially shielded using 80-nm-thick electron-beam-patterned PMMA layers (Figure 4A,B) and a 500-nm-thick S1805 photoresist (Figure 4C–F; details in the Experimental Section). The text structure (Figure 4A) and interconnected grid (Figure 4B) were developed in 120 s, which illustrates that the gold particles can be deposited with 60 nm lateral resolution without finding any particles on the resist itself. This is quite remarkable, again showing that the insulating surfaces appear to self-equilibrate to a sufficiently high potential for the nanoparticle flux to be directed only to grounded regions. A focusing effect and a small standard deviation in the location of the deposits become apparent using 1 μm circular openings (Figure 4C–E). Here, the particles initially deposit into an area that is approximately seven times smaller than the opening but spread out over time,

small NANO MICRO

to yield towerlike structures that can be several micrometers tall (Figure 4D). This focusing effect is a function of the deposition rate and needs to be further investigated. Higher deposition rates appear to defocus the patterns. Continued deposition causes the tops of the towers to broaden (Figure 4E). These towers contain several hundred layers of 5–20-nm particles. Small 1-μm deposits (Figure 4A,B) are uniform over large areas, while tall 2-μm deposits (Figure 4F) begin to show some level of variation over millimeter-sized areas.

Initial focusing of deposited nanoparticles (Figure 4G) has been observed previously when a surface was exposed to ions and a low concentration of nanoparticles.[30] The relative precision of focused nanoparticle deposition was found to depend on the insulator surface potential.[30] The initial deposition behavior is sufficiently similar to prior work to prompt a brief discussion of the deposition physics. Here, the observed focusing effect and expected precision can be studied by solving Langevin's equations of motion of nanoparticles inside an electric field. To establish an analytical form for the relative precision, we considered a single particle at a radial distance r from the center of a patterned hole, as illustrated in Figure 4G. In this case, the uncertainty acquired in the particle trajectory (Δr) due to Brownian motion can be described by the root-mean-square displacement or half-width of the Gaussian bell curve $\Delta r = \sqrt{(2\Delta t D)}$, where Δt is the time for a particle to deposit and $D = CkT/(3\pi d\eta)$ is the Stokes–Einstein diffusion coefficient for nanoparticles of diameter d, viscosity η, and empirical slip correction factor C. Maximum deviation considering a Newtonian trajectory will occur at the center, where the field strength is smaller and where the time to deposit will be increased. The electric field along the central particle path, $E_s = \Delta V/(\pi r)$, will cause the particle to follow the trajectory with a terminal velocity $v_t = CqE_s/(3\pi d\eta) = qE_s D/(kT)$. Substituting $\Delta t = r/v_t$ yields a normalized half-width of the Gaussian bell curve in the form of Equation (1):

$$\frac{\Delta r}{r} = \sqrt{\frac{2kT}{qrE_s}} = 2.507\sqrt{\frac{kT}{q\Delta V}} \quad (1)$$

Equation (1) provides a number of important insights into electric-field-directed self-assembly processes. First, the key measure of the expected focusing will be the potential difference between charged and uncharged areas. Values of $q\Delta V$ larger than kT are desired. Second, the relative precision is independent of the size of the pattern and therefore scaleable. Third, the precision can be increased by increasing the particle charge.

Following initial focused deposition, the process is allowed to continue until deposited conductive nanoparticles eventually alter the electric field lines. The towers grow with electric field lines pointing towards the tops of the nanoparticle towers, which exceed the height of the confining charged resist. Due to this increased distance between depositing nanoparticle and charged resist, nanoparticle mass transport becomes more poorly focused to the center of the resist openings, which results in mushroom-shaped nanomaterial towers.

Figure 5 shows the process and results of programmable deposition of three different materials, Au, ZnO, and Ge, using sequentially biased electrodes, and the concept of programmable deposition is applied to produce a multimaterial sensor array with humidity and photosensitive regions. The

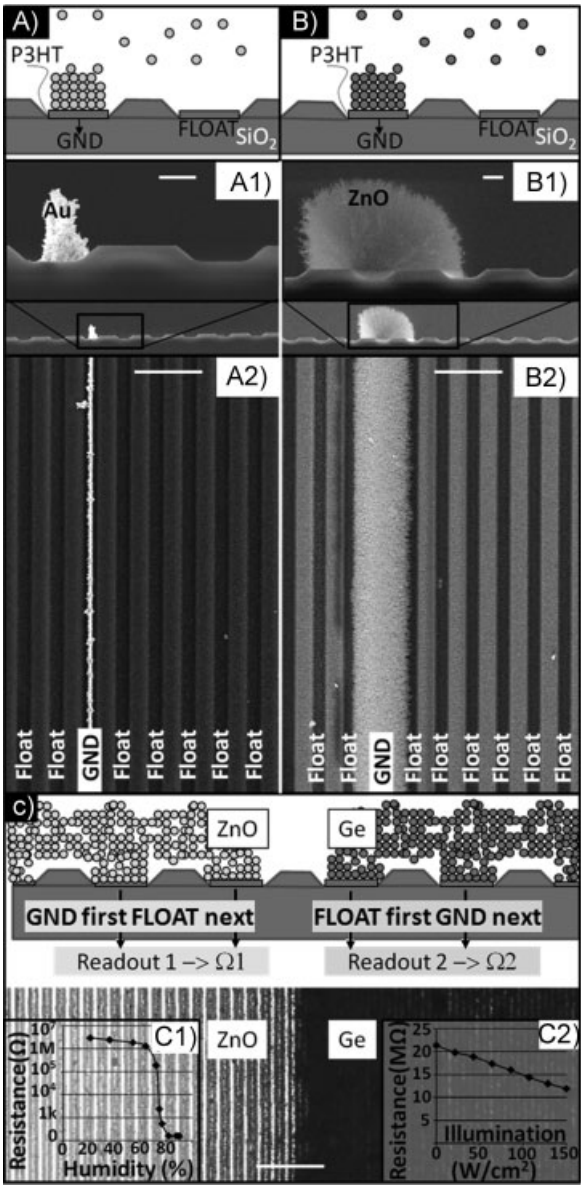

Figure 5. Concept and results of programmable multimaterial (Au, ZnO, Ge) deposition forming A) conducting and B) semiconducting traces, or C1) humidity- and C2) light-sensitive areas. A,B) Grounded 1-μm-wide P3HT lines attract nanoparticles to form a continuous interconnected structure, as illustrated in the cross-sectional (A1,B1) and top-down (A2, B2) SEM images. Au particles pack into denser structures than ZnO and yield smaller line widths for an identical deposition time (30 min) and arc power (10 W). C) Programmable deposition procedure using sequentially grounded electrodes applied to form sensing layers, where the same electrodes are subsequently used for readout. During the first deposition cycle, all the electrodes on the left-hand side are connected to ground until ZnO forms a merged film on the left side. This is reversed in the second cycle to the right until Ge covers the right-hand side of the chip, which is visible in the darker appearance of Ge under an optical microscope. The two film regions bridge the electrodes underneath and yield a characteristic resistance, which reduces with humidity for ZnO (C1) and with illumination for Ge (C2). Scale bars: (A1,B1): 1 μm, (A2,B2): 10 μm, and (C): 20.

illustrations (Figure 5A–C) depict the concept. First, gold nanoparticles are plated on a grounded organic conductor comprising poly(3-hexylthiophene) (P3HT), while nearby P3HT lines and glass surfaces (preparation details in the Experimental Section) electrically float up to a sufficiently high electrical potential, thus preventing gold-nanoparticle deposition in the surrounding area. The resistance measured for the initial P3HT line exceeded 10 MΩ. Covering the P3HT line with Au nanoparticles reduced the resistance to 2.9 kΩ. The Au line was 3 mm long, ≈500 nm wide, and plated be 1 μm thick. Application of Ohm's law yields a measured resistivity of $4.8 \times 10^{-5}\,\Omega\,\mathrm{cm}$, which is close to $2.26 \times 10^{-6}\,\Omega\,\mathrm{cm}$ (the accepted value for Au at 298 K). After Au line deposition, the arc electrodes are replaced to deposit ZnO onto a separate, originally floating P3HT line, which is now grounded while everything else is left floating (Figure 5B). ZnO nanoparticles now deposit selectively onto the grounded electrodes as before in the case of Au. The ZnO example illustrates what happens after 30 min of deposition. The films begin to overgrow the grounded region and form a roughly hemicylindrical structure.

This concept of programmable deposition and overgrowth bridging nearby electrodes can be used to program the deposition of multimaterial sensor arrays while providing a parallel readout on a single chip. The concept is illustrated for ZnO and Ge in Figure 5C, which results in a continuous interconnected film of ZnO on the left and Ge on the right. The films bridge adjacent conductive lines (preparation details in the Experimental Section) whereby the bridge resistance varies with exposure to light (Ge) and humidity (ZnO). The magnitude of the resistance change in Ge due to illumination is attributed to long minority carrier lifetimes in the crystalline Ge. The large increase in the conductivity for ZnO is most likely directly related to the high porosity and large surface area, which is apparent in the cross-sectional SEM image (Figure 5B1) discussed before.

To understand why a uniform deposition is observed and what the potential limitations might be, the thickness of the space-charge sheaths surrounding the sample surface has to be considered. These sheaths are depicted in Figure 3D and are analogous to the double layers surrounding the surfaces in the liquid phase; the thicknesses are on the order of the Debye length.[29] Adjacent areas on the sample within the distances of the characteristic Debye length will compete to attract nanoparticles that arrive at this boundary layer primarily driven by diffusion.[31] As in the liquid phase, the Debye radius r_D is inversely proportional to the square root of the average number concentration n_0 of charged particles above the sample surface, and is given for the gas phase by Equation (2):

$$r_D = \sqrt{\frac{1}{n_0}}\sqrt{\frac{k\varepsilon_0}{e^2(1/T_e + 1/T_i)}} \quad (2)$$

In Equation (2), k is the Boltzmann constant, ε_0 is the free space permittivity, and e is the elementary charge. T_e and T_i are the electron and ion temperatures, respectively, which are assumed to be at room temperature in the aerosol regime. The number concentration n_0 of charged particles that can be supported was estimated using conductivity measurements as described in the Supporting Information, by controlling the distance to the arc and the arc current. Typical values ranged between 10^9 and $10^7\,\mathrm{cm}^{-3}$, which corresponds to a Debye length in the range of 50–500 μm. These n_0 values are close to previously published values of ($10^9\,\mathrm{cm}^{-3}$) recorded near charging sources in atmospheric-pressure aerosols.[32] The numbers are in contrast to the situation in standard vacuum deposition systems, where the Debye length easily exceeds the dimensions of the deposition system by orders of magnitudes since the number concentration of gas molecules drops proportionally with pressure. At the same time the Debye length remains orders of magnitudes larger than the submicrometer values found in the liquid phase. Despite this important difference it has become small enough to enable in situ selected-area deposition. While adjacent areas on the sample compete for nanoparticles within the Debye radius, the formation of arbitrary patterns (Figure 4) can still be achieved. The implication of a sufficiently small Debye length attained at high pressure is that the electrostatic deposition behavior becomes decoupled from the source. Less stringent requirements for symmetric designs with respect to the particle source are a direct result.

Figure 6 investigates the presence of stray particles by testing the deposition on isolated lines and interdigitated

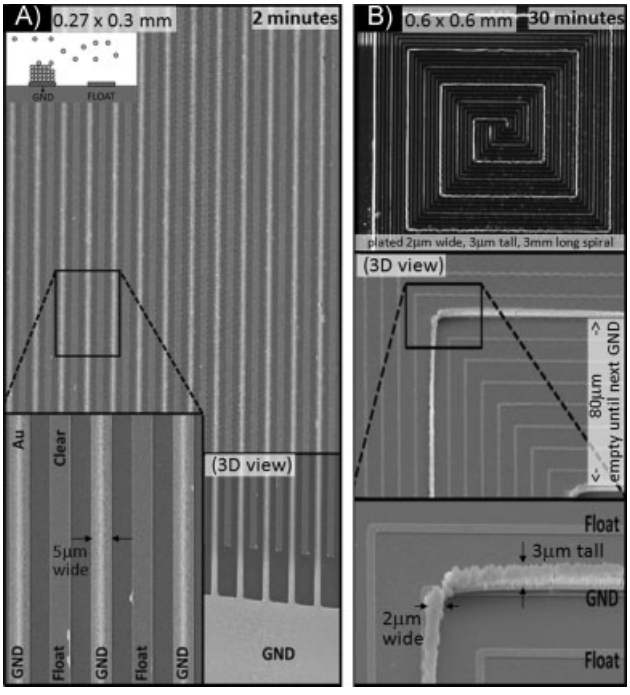

Figure 6. Schematic and results of programmable selected-area gas-phase electrodeposition after 2 (A) and 30 min (B) of deposition. The pad region in (A) (bottom inset) shows the level of uniformity transitioning from a large ($150 \times 150\,\mu\mathrm{m}^2$) single domain to spatially separated 5-μm-wide lines. Deposition occurs only on grounded areas; floating conductors and insulating surfaces remain empty. Increasing the size of the empty regions from 15 (A) to 80 μm (B) maintains this selectivity. The optical microscope image (B) depicts a spiral interspaced with seven empty regions that were left floating, to yield a single 2-μm-wide, 3-μm-tall, and 3-mm-long Au line.

small NANO MICRO

electrode structures. The dimensions of the patterns are scaled to provide a larger field of view showing 15-μm (Figure 6A) and 80-μm (Figure 6B) pitched patterns. Nanoparticle deposition selectivity is high: even after extended deposition times these test structures did not produce an observable number of stray particles on the insulating surfaces or floating metal lines. The correctly deposited Au was 3 μm tall, which represents at least 100 particle layers. We expect the selectivity of sequential deposition steps with multiple material types to be nearly as high as the selectivity of a single step, since crosstalk between lines appears to be minimal.

3. Conclusions

Comparable to liquid-phase electrodeposition, the reported gas-phase analogue can deposit material into addressable areas to form vias, interconnects, or patterned multimaterial films in a programmable fashion. The process was tested using a limited set of technologically relevant functional materials including Au, Si, Ge, TiO_2, and ZnO at sizes of 20 nm and below, as confirmed by TEM, SAED, EDX, and XRD. We anticipate that the process can be extended to other materials and gas-phase systems with some alterations. The uniformity on a macroscale is presently limited by diffusion since we use a single-point source fixed in space. Scaling to larger sample areas would require the use of either multiple sources or translational motion analogous to what has been used in other gas-phase deposition systems. The ability to maintain uniformity when developing arbitrary patterns on the nanoscale requires a sufficiently small Debye length, which in turn favors higher-pressure aerosols to provide a high concentration of charged particles/ions and increased deposition rate. The estimated values are sufficient to support selected-area programmable deposition of a variety of different patterns, including text and connected and disconnected structures. Operating a system at atmospheric pressure has the advantage of simplicity since neither vacuum pumps nor high-pressure enclosures are required. Pressurized systems, however, would most likely further increase the area-selective deposition rate beyond the current 100 nm min^{-1} value. The present area-selective rate is in between the 10 nm min^{-1} rate of nonselective vacuum deposition systems and the typical 1 μm min^{-1} rate of area-selective electroplating methods. Variations in the film thickness, extension to large-area deposition using multiple spatially separated discharge regions, and passivation of surface and interface states are important aspects that will require further research and new, improved designs.

A potential future application of the gas-phase electrodeposition technique can be found in the field of printable electronics. It contrasts the use of solution-processable electronic inks and inkjet-type printing concepts to deposit nanomaterials. Current inkjet-based deposition systems have low resolution and throughput. The inks require surface functionalization to stabilize the particles, which often interferes with the desired electronic properties. Alternatively, the discussed in situ gas-phase synthesis and deposition system offers a more parallel route to the formation, deposition, and integration of higher-performance materials than liquid-phase concepts. High-temperature processes can be used to produce materials that can then be deposited onto low-temperature substrates, thus eliminating any extra processing steps or a transition into the liquid phase. As such, the present technique is highly parallel and does not require the use and alignment of scanning nozzles or the formulation of stable liquid particle suspensions. These advantages come at the cost of needing prepatterned substrates to direct the deposition.

4. Experimental Section

Nanoparticle deposition system: The apparatus was enclosed in a sealed polypropylene desiccator to prevent nanoparticle inhalation and to provide an inert experimental environment (Ar, He, and N_2 gases). We used a 10 kV, 100 mA controlled-current power supply (Gamma High Voltage Research Inc., 1 kW model RR5-120R/CPC/M994) to ignite and maintain a 1–100 W dc arc discharge between two identical consumable electrodes. For consumable electrode materials we used Au, Ti, or Zn in wire form (2 to 5 mm in diameter) and Si and Ge wafer segments 4 cm long and 1 cm wide. The materials were attached using a slit-type clamp cut into 15-mm-diameter copper rods that allowed the separation to be adjusted.

Substrates for selected-area deposition: Patterned PMMA layer (Figures 3F,G and 4A,B) and 500-nm-thick S1805 photoresist sections were used to define the resist openings. A brief 49% HF wet etch 30 s in duration was used to remove the native silicon oxide layer. Samples were thoroughly rinsed with deionized water, blown dry by ultrahigh-purity nitrogen (99.998%), and allowed to rehydrate for up to 15 min in ambient-humidity environments typically ranging from 10 to 20% as measured by a humidity probe (Fisher Scientific, model S11120). Results are shown in Figures 3 and 4.

Substrates for programmable selected-area deposition: Plasma-enhanced chemical vapor deposition was used to coat a Si substrate with 500 nm SiO_2. The SiO_2 layer was patterned by photolithography and plasma-etched by a mix of CF_4, CHF_3, and Ar at a power of 150 W. The plasma etch was used to generate the trench features, such that even at the bottom of the trenches SiO_2 remained. The photoresist was finally stripped. Following SiO_2 patterning, the substrate was covered with a thick layer of P3HT, which was carefully etched back by O_2 plasma reactive-ion etching until only P3HT in the trenches remained. Results are shown in Figure 5A and B.

Substrates for multimaterial sensor formation: Cr/Cu (20/200 nm) was evaporated onto a photolithographically patterned Pyrex wafer. Undesired Cr/Cu was removed by lift-off with acetone acting as the resist stripper and sonication to aid the process. The remaining metal was rinsed with methanol and isopropyl alcohol. Then the substrate was exposed to an oxygen plasma descum to remove any resist residue. Finally, the substrate was rinsed with deionized water and blown dry with N_2 to remove any dust particles before nanoparticle collection. Results are shown in Figure 5C.

Acknowledgements

The authors acknowledge support of this work by NSF DMI-0755995, NSF DMI-0621137, and NSF DMI-0556161. We also acknowledge NSF ECS-0407613 for early seed support. We thank W. Peria and J. Heberlein for input and discussions.

[1] K.-J. Jang, J.-M. Nam, *Small* **2008**, *4*, 1930.
[2] R. A. Barry, III, R. F. Shepherd, J. N. Hanson, R. G. Nuzzo, P. Wiltzius, J. A. Lewis, *Adv. Mater.* **2009**, *21*, 2407.
[3] G. M. Gratson, F. Garcia-Santamaria, V. Lousse, M. Xu, S. Fan, J. A. Lewis, P. V. Braun, *Adv. Mater.* **2006**, *18*, 461.
[4] M. A. Meitl, Z.-T. Zhu, V. Kumar, K. J. Lee, X. Feng, Y. Y. Huang, I. Adesida, R. G. Nuzzo, J. A. Rogers, *Nat. Mater.* **2006**, *5*, 33.
[5] T. A. Kravchenko, M. Y. Chayka, D. V. Konev, L. N. Polyanskiy, V. A. Krysanov, *Electrochim. Acta* **2007**, *53*, 330.
[6] M. Sun, G. Zangari, M. Shamsuzzoha, R. M. Metzger, *Appl. Phys. Lett.* **2001**, *78*, 2964.
[7] D. Bera, S. C. Kuiry, S. Patil, S. Seal, *Appl. Phys. Lett.* **2003**, *82*, 3089.
[8] T. Ohgai, I. Enculescu, C. Zet, L. Westerberg, K. Hjort, R. Spohr, R. Neumann, *J. Appl. Electrochem.* **2006**, *36*, 1157.
[9] Y. Liu, L. Wu, P. T. Lai, Q. Zuo, *Semicond. Sci. Technol.* **2009**, *24*, 095013/1.
[10] Y. Qiu, Y. Hu, G. Dong, L. Wang, J. Xie, Y. Ma, *Appl. Phys. Lett.* **2003**, *83*, 1644.
[11] A. Jaworek, A. Krupa, T. Czech, *J. Electrostat.* **2006**, *65*, 133.
[12] W. Kraetschmer, L. D. Lamb, K. Fostiropoulos, D. R. Huffman, *Nature* **1990**, *347*, 354.
[13] S. Iijima, *Nature* **1991**, *354*, 56.
[14] T. W. Ebbesen, P. M. Ajayan, *Nature* **1992**, *358*, 220.
[15] C. Journet, W. K. Maser, P. Bernier, A. Loiseau, M. Lamy de la Chapells, S. Lefrant, P. Deniard, R. Lee, J. E. Fischer, *Nature* **1997**, *388*, 756.
[16] W. Han, P. Redlich, F. Ernst, M. Ruhle, *Appl. Phys. Lett.* **2000**, *76*, 652.
[17] D. Bera, S. C. Kuiry, M. McCutchen, A. Kruize, H. Heinrich, M. Meyyappan, S. Seal, *Chem. Phys. Lett.* **2004**, *386*, 364.
[18] S.-M. Liu, M. Kobayashi, S. Sato, K. Kimura, *Chem. Commun.* **2005**, 4690.
[19] C. R. Barry, N. Z. Lwin, W. Zheng, H. O. Jacobs, *Appl. Phys. Lett.* **2003**, *83*, 5527.
[20] D. H. Tsai, S. H. Kim, T. D. Corrigan, R. J. Phaneuf, M. R. Zachariah, *Nanotechnology* **2005**, *16*, 1856.
[21] Characteristic spectral emission from pure Ar discharges includes red-purple emission peaks at 697 nm due to ionization of Ar molecules into Ar^+ and at 481nm for Ar^{++}, while blue-white O_2 discharges contain ionized peaks at 419 nm due to $O_2{}^+$ and at 646 and 777 nm due to the dissociation of the O_2 molecule into atomic O. The noble gases that we used to provide the inert environment discussed later (Ar, He) show similar basic arc characteristics and are also known to release electrons by charging to a positively ionized state.
[22] B. M. Smirnov, *Physics of Ionized Gases*, Wiley, New York **2001**.
[23] High-current 100 A arc discharges, classically referred to as high-temperature thermal plasmas or plasma sprays, describe a case where the electrons and ions are in thermal equilibrium and sufficiently hot to quickly evaporate the cathode material. However, erosion and the production of nanoparticles has been reported even under corona discharge conditions, which sustain much smaller currents, typically less than 500 μA. The input power used in the experiments reported here ranged between 1 and 100 W with controlled arc currents of less than 100mA, which is quite similar to what is used in atmospheric-pressure arc discharge lamps. We anticipate that higher current levels are most likely going to work as well.
[24] The consideration that nanoparticles originate from the grounded cathode and do not deposit on insulating surfaces leads to the conclusions that Coulomb forces dominate the deposition process and that nanoparticles charge to be unipolar prior to deposition on the sample electrode. If neutral particles were present they would coat the insulating surfaces and this is not the case. If the aerosol were to have both positively and negatively charged particles above the sample surface, we would again anticipate that the insulating surface would build up a particle layer, contrary to observation. The material flux forming the deposits (Figure 3F,G), together with the recorded positive-ion current and absence of deposition on the insulating surfaces, can only be explained if the nanomaterials are predominantly positively charged. Insulating surfaces are initially uncharged and we would expect a limited amount of charged material to deposit until the insulator fully charges. Such deposition is not observed within the ≈5 nm resolution limit of our SEM instrument. This behavior can be explained if we consider the higher mobility of gas ions when compared to nanoparticles. Gas ions such as Ar^+ in Figure 3 are likely to be responsible for establishing an equilibrium charge and potential distribution as the experiment is started. As indicated in Figure 3C, Ar^+ ions surrounding the insulator are expected to be responsible for preventing deposition of the positively charged M^+ nanoparticles on the insulator.
[25] Sheath regions (purple near cathode and green near anode in Figure 5A) are confined to distances on the order of the Debye length of the high-mobility electrons in the system. The anode sheath accumulates a negative space charge dominated by high-mobility electrons, whereas the cathode sheath is depleted of free electrons yielding a positive space-charge region of primarily Ar^+ ions when considering the depicted argon plasma situation. We refer to Lichtenberg et al.[27] for detailed calculations of the sheath region at the cathode of an arc discharge lamp. The Debye length is $r_D = \sqrt{[(k \times \varepsilon_0/e^2)(T_e/n_e)]}$, where k is the Boltzmann constant (8.62×10^{-5} eV K^{-1}) and ε_0 is the permittivity of free space (8.854×10^{-12} F m^{-1}), and this electrostatic shielding length depends on the ratio between the electron temperature T_e and electron concentration n_e. The range of possible values is great: $n_e = 10^{16}$ cm^{-3}, $T_e = 22000$ K, and $r_D = 200$ nm are common for a high 6 A atmospheric-pressure arc, whereas $n_e = 10^8$ cm^{-3}, $T_e = 11600$ K, and $r_D = 0.7$ mm have been discussed for a lower-current corona discharge.
[26] L. Dabringhausen, D. Nandelstadt, J. Luhmann, J. Mentel, *J. Phys. D: Appl. Phys.* **2002**, *35*, 1621.
[27] J. Luhmann, S. Lichtenberg, O. Langenscheidt, M. S. Benilov, J. Mentel, *J. Phys. D: Appl. Phys.* **2002**, *35*, 1631.
[28] W. C. Hinds, *Aerosol Technology*, Wiley, New York **1999**.
[29] A. Fridman, L. A. Kennedy, *Plasma Physics and Engineering*, Taylor & Francis, New York **2004**.
[30] C. R. Barry, H. O. Jacobs, *Nano Lett.* **2006**, *6*, 2790.
[31] The competition between neighboring areas attracting materials within the Debye radius could in principle affect the deposition rate. However, we have not been able to increase the deposition rate on going from a dense pattern to an isolated line, which suggests that diffusion plays a role in the observed uniformity.
[32] F. J. Romay, B. Y. H. Liu, D. Y. H. Pui, *Aerosol Sci. Technol.* **1994**, *20*, 31.

Received: August 18, 2009
Revised: February 17, 2010

